INTERNATIONAL JOURNAL FOR NUMERICAL AND ANALYTICAL METHODS IN GEOMECHANICS
Int. J. Numer. Anal. Meth. Geomech., 2003; **27**:425–451 (DOI: 10.1002/nag.280)

Capturing strain localization behind a geosynthetic-reinforced soil wall

Timothy Y. Lai, Ronaldo I. Borja*,†, Blaise G. Duvernay and Richard L. Meehan

Department of Civil and Environmental Engineering, Stanford University, Stanford, California 94305, USA

SUMMARY

This paper presents the results of finite element (FE) analyses of shear strain localization that occurred in cohesionless soils supported by a geosynthetic-reinforced retaining wall. The innovative aspects of the analyses include capturing of the localized deformation and the accompanying collapse mechanism using a recently developed embedded strong discontinuity model. The case study analysed, reported in previous publications, consists of a 3.5-m tall, full-scale reinforced wall model deforming in plane strain and loaded by surcharge at the surface to failure. Results of the analysis suggest strain localization developing from the toe of the wall and propagating upward to the ground surface, forming a curved failure surface. This is in agreement with a well-documented failure mechanism experienced by the physical wall model showing internal failure surfaces developing behind the wall as a result of the surface loading. Important features of the analyses include mesh sensitivity studies and a comparison of the localization properties predicted by different pre-localization constitutive models, including a family of three-invariant elastoplastic constitutive models appropriate for frictional/dilatant materials. Results of the analysis demonstrate the potential of the enhanced FE method for capturing a collapse mechanism characterized by the presence of a failure, or slip, surface through earthen materials. Copyright © 2003 John Wiley & Sons, Ltd.

KEY WORDS: constitutive relations; deformation; earth pressures; failure; geosynthetics; numerical modelling; plasticity; retaining walls; strain localization

INTRODUCTION

Strain localization is now generally recognized as a major factor governing the overall response of structures at or near failure. In geomaterials, it occurs under various stress conditions, from the simple case of uniaxial compression of cylindrical soil and rock specimens, to behaviour as complex as subsurface geologic faulting capable of triggering large earthquakes. Over the last few years research on this topic has grown at a very rapid pace both in the laboratory testing aspect as well as in the development of theoretical models and numerical algorithms [1–14].

Strain localization manifests itself in the form of a shear band, a narrow zone of intense straining. It is now generally recognized that the intense deformation in the shear bands is

*Correspondence to: R. I. Borja, Department of Civil and Environmental Engineering, Stanford University, Stanford, California 94305, USA
†E-mail: borja@stanford.edu

Contract/grant sponsor: National Science Foundation; contract/grant number: CMS-9700426

 Received 1 August 2002

primarily responsible for the accelerated softening response exhibited by most structures at post-peak strength. Strain localization is caused by the imperfections inherent in the medium, the boundary constraints, and non-uniform loading conditions. An ideal solution would capture all of these imperfections and irregularities in the mathematical model, but this may not be possible since these defects and irregularities are usually unknown to the analyst. An alternative approach would be to treat this problem as material instability and determine conditions under which the governing equations of equilibrium could admit more than one solution. This latter approach is pursued in this paper.

A numerical model has been developed fairly recently that accommodates localized deformation in a finite element (FE) analysis. The model is based on an embedded strong discontinuity approach [15–18] and allows accurate resolution of the shear band even with a relatively coarse mesh. The term 'strong discontinuity' refers to a particular regularization procedure in which the shear band thickness is assumed to be zero, thus circumventing the issue of length scale in FE analysis. In most geotechnical applications, this is a reasonable assumption since the typical thickness of the shear band is many orders of magnitude smaller than the dimensions of the structure. Furthermore, the embedded discontinuity approach allows the steep gradients across the shear band to be captured accurately by the FE solution without having to severely refine the mesh. The embedded discontinuity approach has been used in Reference [19] to study strain localization in rocks, and in Reference [20] to investigate the propagation of shear bands behind a rigid retaining wall.

In this paper, we demonstrate the capability of the embedded strong discontinuity approach to capture the collapse mechanism behind a geosynthetic-reinforced soil (GRS) wall. The particular case study analysed in this paper involves a 3.5-m tall full-scale GRS wall model deforming in plane strain and loaded by surface surcharge to failure. Details of the full-scale model and experiments are presented in Reference [21]. Important factors that have led to the selection of this particular experiment as a benchmark test for the strain localization model included the fact that: (a) it is a full-scale test, which is preferred to a small-scale test; (b) the experimental conditions are very close to plane strain, the condition for which the strain localization model has been implemented; (c) a distinct failure surface developed during testing; (d) the facing is continuous, which is preferred to a segmental facing for model simplicity; (e) relevant material parameters and model dimensions are available; (f) the boundary conditions are clearly defined, including the extent of the soil backfill and (g) measurements of all relevant parameters, such as the applied loads, deformations, forces, pressures, strains and geometry of the failure surface are complete and accurate.

Other important elements of the analysis include an accurate representation of the interaction between the geosynthetics and the surrounding soil. Furthermore, a combination of load-controlled and displacement-controlled numerical simulation is used to advance the solution near the global collapse state, where the tangent operator is nearly singular. The numerical results clearly demonstrate the shortcomings of standard FE solutions in capturing the collapse mechanism and the post-localization responses, and underscore the key role played by the embedded strong discontinuity approach in the FE modelling of the intense deformation occurring in the soils behind the test wall.

The notations and symbols used throughout this paper are as follows: bold-face letters denote matrices and vectors; the symbol '·' denotes an inner product of two vectors (e.g. $\mathbf{a} \cdot \mathbf{b} = a_i b_i$), or a single contraction of adjacent indices of two tensors (e.g. $\mathbf{c} \cdot \mathbf{d} = c_{ij} d_{jk}$); the symbol ':' denotes

an inner product of two second-order tensors (e.g. $\mathbf{c} : \mathbf{d} = c_{ij}d_{ij}$), or a double contraction of adjacent indices of tensors of rank two and higher (e.g. $\mathbf{C} : \boldsymbol{\epsilon}^{\mathrm{e}} = C_{ijkl}\epsilon^{\mathrm{e}}_{kl}$).

FE METHOD WITH EMBEDDED DISCONTINUITY

The objective of the embedded discontinuity approach in FE modelling of localized deformation is to resolve the steep displacement gradients across the shear band without resorting to severe mesh refinement. This is accomplished by embedding a discontinuity into the finite elements in the form of strain enhancements that reflect the characteristics of the localized region, such as the shear band orientation and the constitutive properties of the material inside the localization zone. The embedded discontinuity can be a layer of finite thickness (called weak discontinuity [8]), or a layer of zero thickness (called strong discontinuity [1]), that is added to the standard FE interpolation to capture the steep displacement gradients that otherwise would not be resolved by the conventional FE interpolation. Embedding a layer of zero thickness into the FE interpolation generally leads to a simpler and more efficient implementation, and hence is used in the present studies.

The calculations proceed as follows. In the beginning of the analysis where the stress level is low, the structure is assumed to deform homogeneously and the conventional FE modelling is used. However, when the stress level becomes high enough, the structural response could bifurcate to a localized mode. The bifurcation point is determined from a local stability analysis, point-by-point (in FE calculations, the stability analysis is done at the Gauss point level). Issues pertaining to localization to planar bands are discussed in Reference [22] within the context of finite deformation. In this paper, we use the infinitesimal formulation of the strong discontinuity theory. Once the condition for the onset of localization has been established, the FE interpolation may be enhanced to capture the localized deformation mode.

The bifurcation analysis entails the solution of an eigenvalue problem which gives the orientation of the shear band. This orientation is used by the FE model to characterize the discontinuity that is subsequently embedded into the FE interpolation. In addition, the constitutive properties of the shear band are also prescribed for the localizing elements. Note that the shear band properties may be entirely different from the properties of the intact continuum. In the model the shear band properties are represented by the mobilized cohesion $c_{\mathscr{S}}$ and the mobilized friction angle $\phi_{\mathscr{S}}$ on the surface of discontinuity.

Figure 1 illustrates why the standard FE approximation fails to characterize the effect of strain localization. When a narrow shear band forms across the element, the resulting displacements are restricted by the requirement that the elements conform with the deformation. Consequently, unless the element sides are oriented in the direction of the shear band and the element thickness is in the same order of magnitude as the thickness of the shear band, the predicted movements will be inaccurate because the elements are unable to capture the strain localization effects. However, by embedding a discontinuity in the elements the capability of the FE method to resolve the intense deformation inside the shear band is greatly enhanced.

MOTIVATIONS FOR ADVANCED FE ANALYSIS OF GRS WALLS

The rapid deployment of geosynthetic technologies has raised new issues in foundation performance that are not fully addressed by conventional FE solutions, including the problem

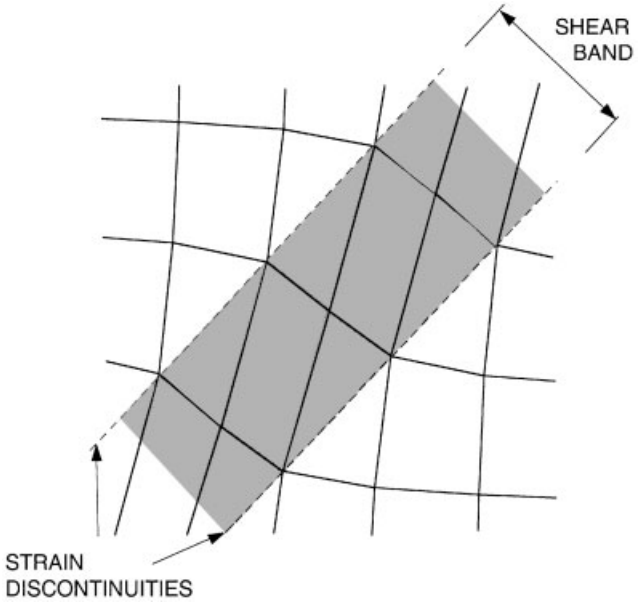

Figure 1. Shear band formation in FE mesh showing dependence of strain discontinuities on mesh resolution.

of strain localization. Accordingly, we have selected a common geosynthetic application as a preliminary test for the proposed strain localization model. In urban areas, GRS walls offer the promise of near vertical grade changes in confined areas at very low cost and are accordingly attractive to land developers where land costs are at a premium. For example, recently proposed projects in Los Angeles feature GRS walls up to 11 m high embedded within 2:1 slopes and supporting apartment buildings and associated urban infrastructure. Building codes applicable to such retaining facilities are immature or absent, though current proposals advanced by trade associations attempt to apply the same limit equilibrium methods used in determination of slope stability analysis [23]. This encourages proposals for increasingly high walls which (it is argued) can be deemed safe because they have high static safety factors.

As in routine foundation design practice, traditional elastic or FE estimates of ground deformation may suffice in some GRS walls to provide a comparison with the empirical settlement guidelines for conventional structures such as housing [24]. Similarly, complications arising from development of ground rupture (i.e., strain localization before full failure) may be avoided by requiring high factors of safety. However, given the trend toward scaling up of GRS walls using relatively low safety factors, it becomes important to realistically anticipate the style as well as increasing magnitude of ground response, particularly where the walls are intended to support structures.

Current research trends in the deformation analysis of GRS walls involve the use of the standard FE method backed in some degree by physical modelling in the laboratory [21, 25–45]. Physical models provide a well-defined FE problem and reduce uncertainties that would otherwise be present in the field, such as those associated with boundary conditions and three-dimensional effects. However, none of the FE models advanced thus far in the literature has

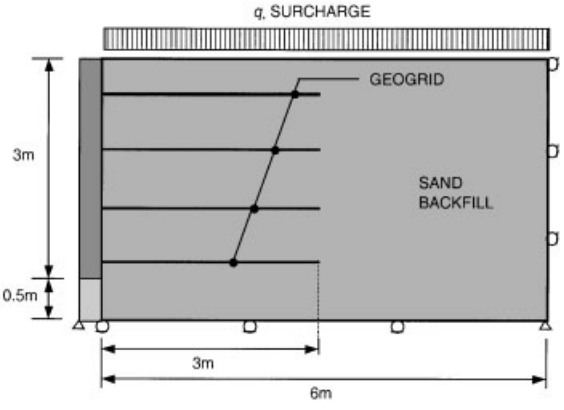

Figure 2. Test configuration showing geogrid layout and boundary conditions.

captured the strain localization effects and the accompanying collapse mechanisms that occurred behind most of the GRS walls tested. Furthermore, there is a great danger with using commercial FE codes employing standard displacement interpolation to infer the behaviour of the structure at or near failure. In the first place, spurious mesh sensitivities are known to afflict the standard FE solutions near the collapse regime, thus rendering the results of the analysis of little value.

The GRS wall used as a benchmark test for the strain localization model is reported in [21] and shown in Figure 2. The setup involved a 6.0 m long by 2.4 m wide and 3.6 m high caisson with rigid low friction lateral walls and a rough concrete slab bottom; the wall facings consisted of a well instrumented, full height, aluminum central panel 1 m wide and two 0.7 m wide edge panels. The central and edge panels were mounted on a leveling pad representing a strip footing and used in field applications to support and align the facing units. The panels were pinned at the base and supported by external props until the full depth of the soil behind the wall has been placed and compacted. The reinforcement consisted of four layers of 3 m long Tensar Geogrid SS1. The backfill material was a uniformly graded sand with some fine gravel placed and compacted in 125 mm lifts. Surcharge load was applied by airbags on the full 2.4 m $\times$ 6 m surface of the backfill by increments of 10 kPa lasting approximately 100 h each. The boundary conditions permit a plane strain characterization of the boundary-value problem.

During the 80 kPa loading episode, failure was observed to initiate in the reinforced soil mass. Inspection revealed a failure scarp in the soil approximately 1 m behind the head of the wall; the surface of the faulted soil mass was observed to have dropped approximately 65 mm. Careful excavation of the backfill revealed an internal failure surface and a ruptured upper layer of geogrid at the connection with the facing. The failure surface had a shape of a log-spiral approximated by a Rankine wedge passing through the toe with corresponding parameters $c = 0$ and $\phi = 53^\circ$.

PRE-LOCALIZATION ELASTOPLASTIC CONSTITUTIVE MODELS

Pre-localization constitutive models describe the mechanical response of a material in the regime of homogeneous deformation. In the context of the present study, the material of interest is a

relatively homogeneous cohesionless sand backfill characterized by a friction angle ϕ and a dilatancy angle ψ, where $\phi \geqslant \psi$ to ensure a nonnegative plastic dissipation [46]. Pre-localization constitutive models only describe the mechanical response of a material prior to the onset of strain localization. However, they are also used to detect bifurcation, or the loss of uniqueness in the solution of the governing boundary-value problem.

In the following we describe candidate plasticity models used to represent the behaviour of cohesionless sands in the regime of homogeneous deformation. We compare the deformation and localization properties of these constitutive models, and then select an appropriate model for the strain localization analysis of the GRS wall case study. Note that all of these plasticity models are smooth versions of the Mohr–Coulomb plasticity model. The latter model is easier to implement in a two- dimensional problem, but is tricky and unwieldy to implement in a three-dimensional setting because of corner effects. There was not any documentation on the hardening/softening properties of the sand backfill reported in Reference [21], and so in this paper we shall simply assume perfect plasticity in the constitutive responses.

Model 1. Drucker–Prager (DP) model

A cohesionless Drucker–Prager plasticity model [47] is described by a yield function $\mathscr{F}$ and a plastic potential function $\mathscr{Q}$ of the form:

$$\mathscr{F} = \sqrt{J_2} + \beta \frac{I_1}{3} = 0, \quad \mathscr{Q} = \sqrt{J_2} + b \frac{I_1}{3} \tag{1}$$

where

$$I_1 = \sigma_1 + \sigma_2 + \sigma_3, \quad J_2 = \frac{1}{6}[(\sigma_1 - \sigma_2)^2 + (\sigma_2 - \sigma_3)^2 + (\sigma_1 - \sigma_3)^2] \tag{2}$$

σ_1, σ_2 and σ_3 are the principal stresses, and the continuum mechanics convention is used. The surface of this two-invariant model defines a right circular cone centered about the hydrostatic axis and passing through the stress space origin, see Figure 3. The parameters β and b are related to the friction and dilatancy angles ϕ and ψ via [48]

$$\beta = \frac{1}{\sqrt{3}} \frac{6 \sin \phi}{(3 \pm \sin \phi)}, \quad b = \frac{1}{\sqrt{3}} \frac{6 \sin \psi}{(3 \pm \sin \psi)} \tag{3}$$

where the negative (positive) sign in the denominator pertains to the case where the circular cone passes through the compression (tension) corners of the Mohr–Coulomb yield surface.

Model 2. Lade–Duncan model

The Lade–Duncan (LD) model [49] is described by yield and plastic potential functions of the form:

$$\mathscr{F} = (k_1 I_3)^{1/3} - I_1 = 0, \quad \mathscr{Q} = (k_2 I_3)^{1/3} - I_1 \tag{4}$$

where

$$I_3 = \sigma_1 \sigma_2 \sigma_3 \tag{5}$$

is the third stress invariant. Although the yield surface depends only on I_1 and I_3, it also may be written in terms of all three stress invariants, and hence, the LD model may be classified as a

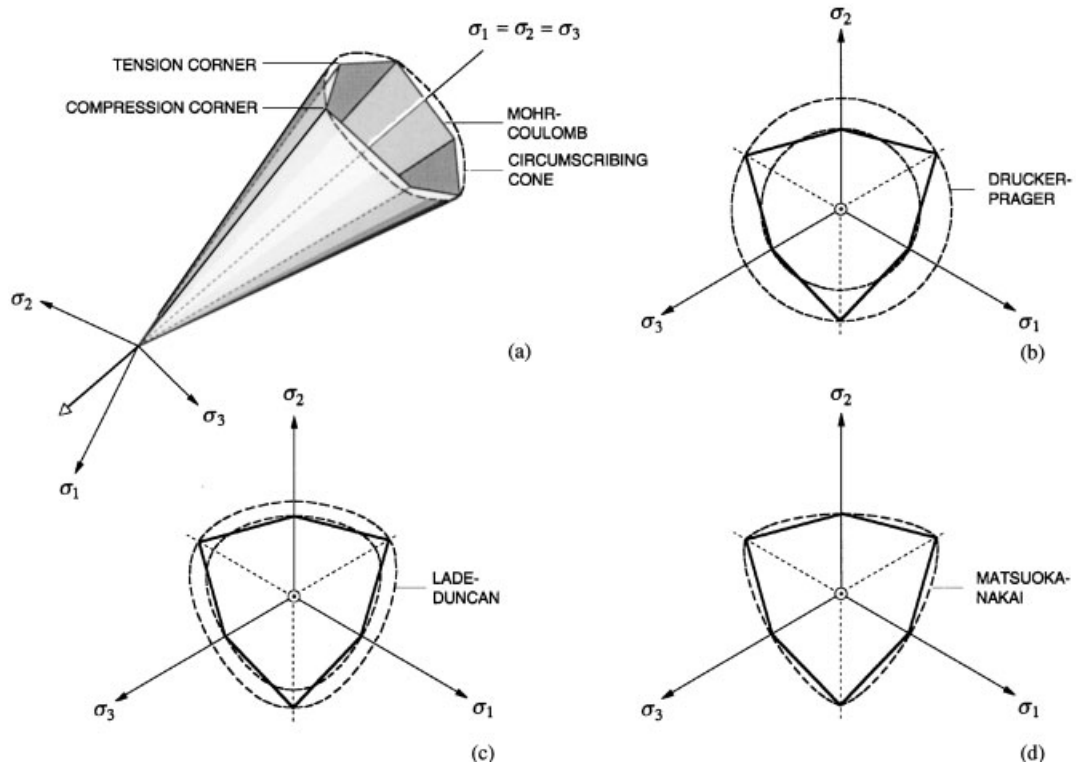

Figure 3. Plasticity models: (a) Mohr–Coulomb yield surface in principal Cauchy stress space; (b) Drucker–Prager representation on octahedral plane; (c) Lade–Duncan; and (d) Matsuoka–Nakai yield surfaces (after References [48, 51]).

three-invariant model. The surface defines a cone similar to the cohesionless DP yield surface except that the cross section is not circular but more closely approximates the Mohr–Coulomb yield surface, see Figure 3. The parameters k_1 and k_2 are related to the friction and dilatancy angles via [48]

$$k_1 = \frac{(3 \pm \sin\phi)^3}{1 \pm \sin\phi - \sin^2\phi \pm (-\sin^3\phi)}$$
$$k_2 = \frac{(3 \pm \sin\psi)^3}{1 \pm \sin\psi - \sin^2\psi \pm (-\sin^3\psi)} \tag{6}$$

where the negative (positive) sign in the plus-or-minus symbols pertains to the case where the cone passes through the compression (tension) corners of the Mohr–Coulomb yield surface. In order for the LD yield surface to contain the hydrostatic axis, $k_1 \geqslant 27$ (which is effectively the same as restricting ϕ to be greater than or equal to zero).

Model 3. Matsuoka–Nakai model

The Matsuoka–Nakai (MN) model [50] is described by yield and plastic potential functions of the form:

$$\mathscr{F} = (\bar{k}_1 I_3)^{1/3} - (I_1 I_2)^{1/3} = 0, \quad \mathscr{Q} = (\bar{k}_2 I_3)^{1/3} - (I_1 I_2)^{1/3} \tag{7}$$

where

$$I_2 = \sigma_1\sigma_2 + \sigma_2\sigma_3 + \sigma_1\sigma_3 \tag{8}$$

is the second stress invariant. The surface of this three-invariant model defines a cone similar to the cohesionless DP and LD yield surfaces but the cross-section now passes through all the compression and tension corners of the Mohr–Coulomb yield surface, see Figure 3. The parameters $\bar{k}_1$ and $\bar{k}_2$ are related to the friction and dilatancy angles via [48]

$$\bar{k}_1 = \frac{9 - \sin^2\phi}{1 - \sin^2\phi}, \quad \bar{k}_2 = \frac{9 - \sin^2\psi}{1 - \sin^2\psi} \tag{9}$$

The restriction $\phi \geqslant 0$ is equivalent to the condition $\bar{k}_1 \geqslant 9$.

An implicit integration of the Drucker–Prager model (or any two-invariant plasticity model for that matter) is well known and is usually carried out by a return mapping in the space defined by the first and second stress invariants. For two-invariant plasticity models with non-linear hyperelasticity, implicit integration may be carried out just as conveniently by a return mapping in the space defined by the first and second strain invariants [52, 53]. Although theoretically a return mapping may be performed in the space defined by all three stress invariants, the third stress invariant has a complicated form in a general six-dimensional stress space and its derivatives are unwieldy to extract. In the comparison of the different constitutive models, we thus utilize a recently proposed technique based on a return mapping in principal stress directions advocated in References [51, 54] for the stress-point integration of the constitutive models capable of accommodating the third stress invariant. As shown in Reference [51], this numerical technique can also handle the curving (or 'flattening') effect of the yield surface with increasing confining pressure [55], although this feature is not utilized in the present numerical simulations.

CONDITION FOR LOCALIZATION

The criterion for the onset of strain localization in the form of a planar shear band is given by (see Reference [56])

$$\det(\mathbf{A}) = 0 \tag{10}$$

where $\mathbf{A}$ is the elastoplastic acoustic tensor with components

$$A_{ik} = n_j c^{\mathrm{ep}}_{ijkl} n_l \tag{11}$$

$\mathbf{c}^{\mathrm{ep}}$ is the elastoplastic constitutive operator, and $\mathbf{n}$ is the unit normal vector to the shear band. In the case of perfect plasticity, this condition also holds for strong discontinuity localization based on the notion of a bounded traction rate [57]. For plane strain localization it is possible to extract a closed-form solution to (10) with the Drucker–Prager model, see Reference [58]. However, such analytical solutions are currently not available for the aforementioned three-

invariant plasticity models, and so to detect the bifurcation point we simply evaluate the determinants numerically for every stress state and for every possible shear band orientation $\mathbf{n}$.

The elastoplastic constitutive operator takes the familiar form:

$$\mathbf{c}^{\mathrm{ep}} = \mathbf{c}^{\mathrm{e}} - \frac{1}{\chi}\mathbf{c}^{\mathrm{e}} : \mathbf{q} \otimes \mathbf{f} : \mathbf{c}^{\mathrm{e}}, \quad \chi = \mathbf{f} : \mathbf{c}^{\mathrm{e}} : \mathbf{q} + H \tag{12}$$

where $\mathbf{f} = \partial \mathscr{F}/\partial \boldsymbol{\sigma}$, $\mathbf{q} = \partial \mathscr{Q}/\partial \boldsymbol{\sigma}$, and H is the plastic modulus (equal to zero in the present case). Although the above form is standard, it leads to an awkward evaluation of $\mathbf{c}^{\mathrm{ep}}$ when combined with the return mapping algorithm in principal stress space for the three-invariant models. An alternative expression for $\mathbf{c}^{\mathrm{ep}}$ is given in spectral form as follows [48, 51]:

$$\begin{aligned}\mathbf{c}^{\mathrm{ep}} = &\sum_{A=1}^{3}\sum_{B=1}^{3} a_{AB}^{\mathrm{ep}}\mathbf{m}^{(A)} \otimes \mathbf{m}^{(B)} \\ &+ \sum_{A=1}^{3}\sum_{B\neq A} \frac{\sigma_B - \sigma_A}{\epsilon_B^{\mathrm{e}} - \epsilon_A^{\mathrm{e}}}(\mathbf{m}^{(AB)} \otimes \mathbf{m}^{(AB)} + \mathbf{m}^{(AB)} \otimes \mathbf{m}^{(BA)})\end{aligned} \tag{13}$$

where σ_A, σ_B are the principal stresses, $\epsilon_A^{\mathrm{e}}, \epsilon_B^{\mathrm{e}}$ are the principal elastic strains,

$$\mathbf{m}^{(A)} = \mathbf{n}^{(A)} \otimes \mathbf{n}^{(A)}, \quad \mathbf{m}^{(AB)} = \mathbf{n}^{(A)} \otimes \mathbf{n}^{(B)} \tag{14}$$

are the spectral directions, and $\mathbf{n}^{(A)}$ is the unit principal direction. The first term of (13) describes the material response in principal axes, in which

$$a_{AB}^{\mathrm{ep}} = a_{AB}^{\mathrm{e}} - \frac{1}{X}\left(\sum_{I=1}^{3} a_{AI}^{\mathrm{e}}\frac{\partial \mathscr{Q}}{\partial \sigma_I}\right)\left(\sum_{J=1}^{3}\frac{\partial \mathscr{F}}{\partial \sigma_J}a_{JB}^{\mathrm{e}}\right) \tag{15}$$

and

$$X = \sum_{I=1}^{3}\sum_{J=1}^{3}\frac{\partial \mathscr{F}}{\partial \sigma_I}a_{IJ}^{\mathrm{e}}\frac{\partial \mathscr{Q}}{\partial \sigma_J} + H \tag{16}$$

where a_{IJ}^{e} represents the elasticity matrix in principal axes. The second term represents the spin of the principal axes [59] and depends solely on the current state of deformation of the material.

The rationale for presenting the above spectral form of the elastoplastic constitutive operator is that the Newton–Raphson method already utilizes this form to evaluate the global tangent operator for the iterative solution of the nonlinear equations, the only difference being that the algorithmic tangent matrix a_{AB} is used in the iterative solution rather than the constitutive tangent matrix a_{AB}^{ep}. Therefore, instead of evaluating the entire constitutive operator $\mathbf{c}^{\mathrm{ep}}$ anew from the more standard form (12), one only needs to assemble the elastoplastic matrix a_{AB}^{ep} in (15) and use it in (13). Alternately, since it is known that the algorithmic matrix a_{AB} approaches the elastoplastic constitutive matrix a_{AB}^{ep} for small load steps, the algorithmic tangent constitutive tensor itself may be used to evaluate the acoustic tensor $\mathbf{A}$ for purposes of detecting bifurcation.

The resulting acoustic tensor takes the form

$$\mathbf{A} = \sum_{A=1}^{3} \sum_{B=1}^{3} a_{AB}^{\mathrm{ep}} \alpha_A \alpha_B \mathbf{n}^{(A)} \otimes \mathbf{n}^{(B)} + \sum_{A=1}^{3} \sum_{B \neq A} \frac{\sigma_B - \sigma_A}{\epsilon_B^{\mathrm{e}} - \epsilon_A^{\mathrm{e}}} (\alpha_B^2 \mathbf{n}^{(A)} \otimes \mathbf{n}^{(A)} + \alpha_A \alpha_B \mathbf{n}^{(A)} \otimes \mathbf{n}^{(B)}) \tag{17}$$

where $\alpha_A = \mathbf{n} \cdot \mathbf{n}^{(A)}$ is the direction cosine of the angle between the shear band orientation vector $\mathbf{n}$ and the unit eigendirection $\mathbf{n}^{(A)}$. In the examples that follow, the principal stresses σ_A and corresponding eigenvectors $\mathbf{n}^{(A)}$ were evaluated iteratively using the IMSL subroutines EVLSF/DEVLSF in Fortran PowerStation 90, see Reference [51].

LOCALIZATION PROPERTIES OF SAND BACKFILL

The objective of this section is to compare the localization properties of the cohesionless sand backfill as predicted by the constitutive models of the preceding section. The soil backfill used in the subject test wall consisted of a uniformly graded sand with some fine gravel. This material had highly angular particles contributing to a high friction angle. Prior to strain localization, the soil was noted in Reference [21] to have a friction angle of $\phi = 53^\circ$ and a dilation angle of $\psi = 15^\circ$; additional parameters used in Reference [21] included a Young's modulus of $E = 35$ MPa (approximated from References [26, 60]) and Poisson's ratio $v = 0.3$ (this value varied during the experiment). The value of Young's modulus is believed to be representative of the averaged stiffness of the soil backfill over the expected range of confining stresses, and is obtained from the averaged initial tangent modulus of the stress-strain curves reported in Reference [27].

The above friction and dilation angles lead to the following DP parameters: $\beta = 1.26$ and $b = 0.33$ for yield/plastic potential surfaces passing through the compression corners, and $\beta = 0.73$ and $b = 0.28$ if passing through the tension corners; LD parameters: $k_1 = 133.3$ and $k_2 = 29.9$ if passing through the compression corners, and $k_1 = 85.6$ and $k_2 = 29.6$ if passing through the tension corners; and MN parameters: $\bar{k}_1 = 23.2$ and $\bar{k}_2 = 9.6$. Strictly speaking, the above friction angle corresponds to failure and not to initial yielding since soils are known to yield right at the onset of loading and thus the true yield friction angle should be very small. Nevertheless, collapse and near-collapse conditions are commonly analysed in practice with the assumption of failure being equivalent to yielding. When combined with a shear band-type stability analysis, however, the assumption that failure is equivalent to yielding may result in some fundamental inconsistencies as elaborated below.

As an illustration we consider a square soil element deforming in plane strain and initially subjected to in-plane normal stresses $\sigma_1 = \sigma_3 = -20$ kPa, and an out-of-plane normal stress $\sigma_2 = v(\sigma_1 + \sigma_3) = -12$ kPa (continuum mechanics convention is used for normal stresses), see Figure 4. The horizontal normal stress σ_3 is held fixed while the magnitude of the vertical compressive stress σ_1 is increased. These stress state and stress path are typical of those experienced by soil elements in the backfill, in which the increase in the vertical compressive stress represents the surcharge loading effect. As shown in Figure 4 the initial stress point does not coincide with the hydrostatic axis, and the stress path tends toward a point near the σ_1-compressive corner of the Mohr–Coulomb yield surface.

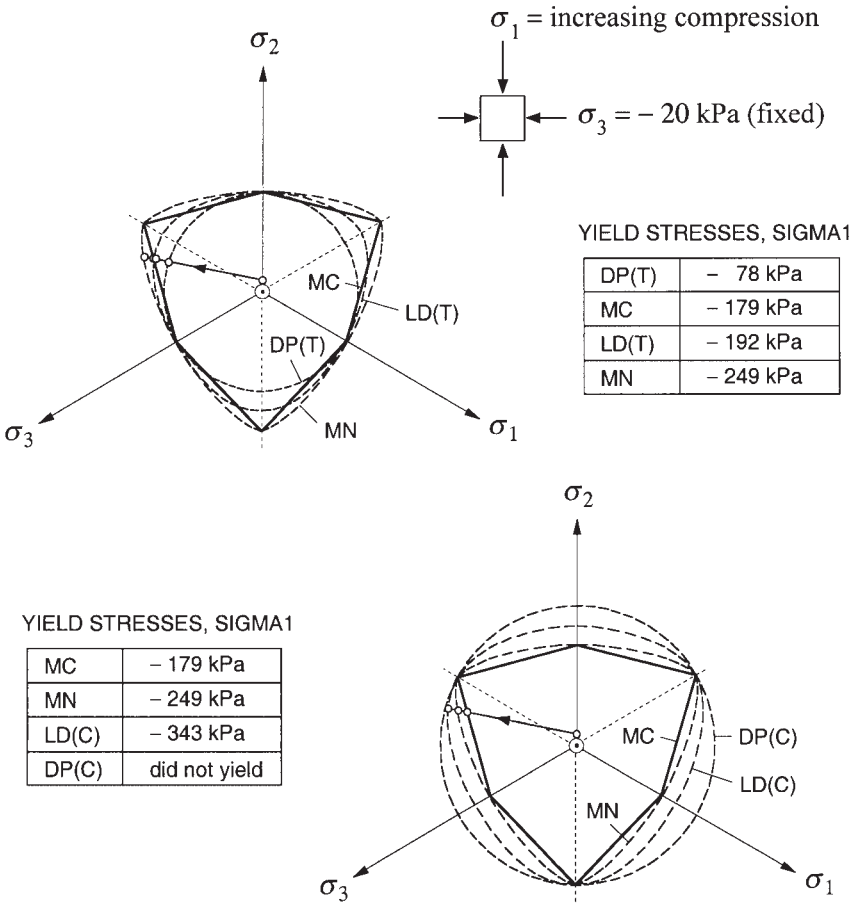

Figure 4. Yield stresses predicted by smooth approximations to the Mohr–Coulomb yield surface for plane strain compression problem: MC = Mohr–Coulomb; DP = Drucker–Prager; LD = Lade–Duncan; MN = Matsuoka–Nakai; (T) = tension corner approximation; (C) = compression corner approximation.

With a known stress path it is possible to determine analytically the stress points at which the different yield surfaces are initially engaged. For the above stress path the sequence of yield surface activation has been observed to be as follows (see Figure 4): DP(T), MC, LD(T), MN, LD(C), and DP(C), where the modifiers (T) and (C) denote tension and compression corner approximations, respectively. Note that the DP(C) yield surface circumscribes all of the yield surfaces, but the DP(T) surface is not fully inscribed in the MC yield surface due to the presence of corners. The MC yield stress is calculated from the standard formula $\sigma_1 = [(1 + \sin\phi)/(1 - \sin\phi)]\sigma_3$, which is not a function of σ_2. Note that the outer Drucker–Prager approximation DP(C) did not allow the soil element to yield because the cone opens up too fast toward the compressive side of the hydrostatic axis that for the given value of Poisson's ratio the elastic stress could not catch up with it.

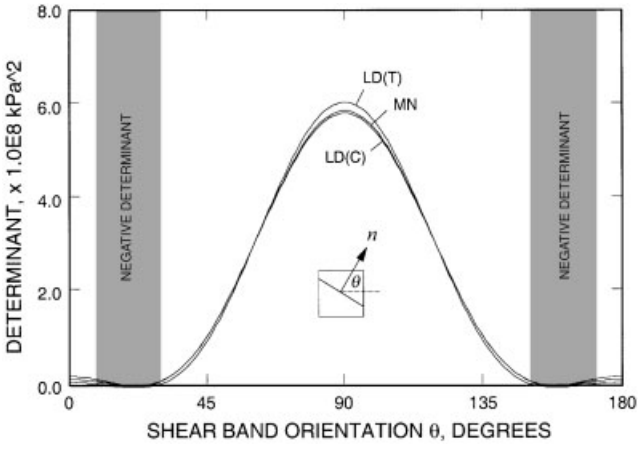

Figure 5. Determinant function versus shear band orientation at initial yield for plane strain compression problem, elastic-perfectly plastic three-invariant models: LD(C) and LD(T) = Lade–Duncan yield surfaces passing through compression and tension corners of Mohr–Coulomb yield surface, respectively; MN = Matsuoka–Nakai surface.

Figure 5 shows the variation of the localization functions (i.e., the determinants of the acoustic tensor) with the shear band orientation θ measured from the horizontal axis at initial contact points for the LD(C), MN, and the LD(T) yield criteria. Note that the calculated localization functions are already negative at some shear band orientation angles when the material was only beginning to yield. Since a negative localization function suggests potential material instability (the tangent constitutive tensor is no longer positive-definite), it would be inappropriate to use the LD or MN yield criteria in combination with the failure friction angle for modelling the pre-localization constitutive behaviour of the backfill sands as these models define elastic regions that extend beyond the boundaries of the 'stable' region. Note that the stable region in this case depends not only on the friction angle but also on the dilation angle of the material at the initial yield point.

Figure 6 plots the localization function versus the angle θ for the DP(T) approximation and shows that at initial yield ($\sigma_1 = -78$ kPa) the determinant of the acoustic tensor is still positive for all possible shear band angles. With increasing compressive stress the determinant vanishes for the first time at a vertical stress of about $\sigma_1 = -138$ kPa at two possible angles, 31° and 149°, corresponding to a shear band oriented at $\pm 59^\circ$ relative to the axis of the minimum principal compressive stress σ_3. This shear band angle (i.e. 59°) is closer to that predicted by the approximate expression $[45^\circ + (\phi + \psi)/4] = 62^\circ$, than to those predicted by either the expression $(45^\circ + \phi/2) = 71.5^\circ$ or the expression $(45^\circ + \psi/2) = 52.5^\circ$, see Reference [61] for a discussion of these approximate formulas. The localization stress of $\sigma_1 = -138$ kPa is also lower than any of the initial yield stresses predicted by the other yield criteria (see Figure 4), and well explains why the calculated tangent constitutive tensors were not positive-definite for these other yield criteria even though the material was just beginning to yield.

While more stress probes may be desirable to ensure that the elastic region defined by the DP(T) yield surface completely lies within the stable region, it appears that the stress state and stress path tested herein are representative enough of those expected in the sand backfill. Hence,

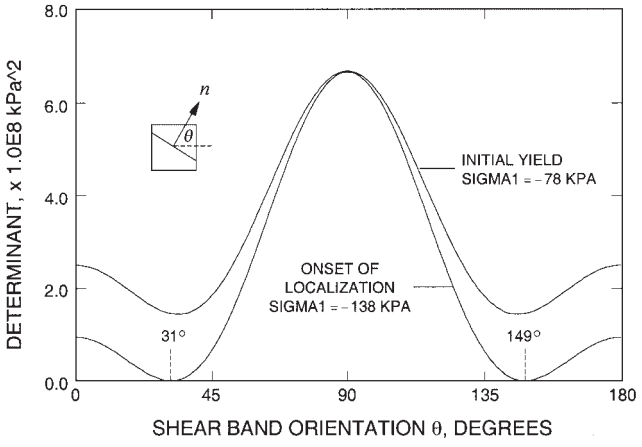

Figure 6. Determinant function versus shear band orientation for plane strain compression problem. Acoustic tensors are evaluated for elastic-perfectly plastic Drucker–Prager model with yield surface passing through tension corners of Mohr–Coulomb yield surface.

we select the DP(T) yield criterion to represent the soil pre-localization constitutive responses in the FE simulation of the subject GRS test wall.

SPECIFICATIONS OF FE MODEL

Three different FE meshes were used in the simulations, shown in Figure 7. Mesh 1 has 142 nodes, mesh 2 has 314, and mesh 3 has 858 nodes. Table I summarizes the features of all three meshes. Two types of elements also have been introduced: linear quadrilateral elements to model the wall and wall-soil interface, and constant strain triangular (CST) elements to model the sand backfill. The geogrids are modelled as axially loaded elements with a linear displacement interpolation similar to those used in Reference [37].

In principle, pullout of the geogrid from the soil must also be modelled, but for the present case study any significant pullout displacement is unlikely. This is because the biaxial geogrid has been oriented in such a way that its weak direction coincides with the direction of loading so that it would rupture first before it pulls out from the soil. Indeed, the topmost geogrid ruptured at the conclusion of the last loading episode and did not pull out [21]. Figure 8 shows a perspective view of the wall-geogrid setup and demonstrates that the soil is continuous through and across a significant area on the plane of the geogrid. The total pullout resistance is the sum of the frictional resistance generated on the contact area between the two materials, as well as from passive bearing resistance of the soil in front of the transverse segments of the geogrid. Because this total pullout resistance is greater than the rupture strength of the geogrid, we assumed that the relative slippage between the soil and geogrid was negligible.

Factors affecting the experiment include the method of construction and type of wall facing. Two types of walls have been tested in Reference [21]. The first wall consisted of four rows of panels and put in place in several stages, designated as an incremental panel wall. The second type of wall consisted of three columns bolted together and set up as a whole, designated as a full-height panel wall. The backfill was put in place in several steps to facilitate compaction.

During this construction stage, the wall was supported externally since the base support allowed for wall rotations. Then, after the geogrid and soil have been set up, and just before surcharging, the external supports to the wall were removed. Our numerical simulation did not attempt to replicate all of the complex stages of construction mentioned above. Instead, we simply assumed that the wall, geogrid, and the soil were already in place, and comparisons were made only to data from the full-height panel wall experiment.

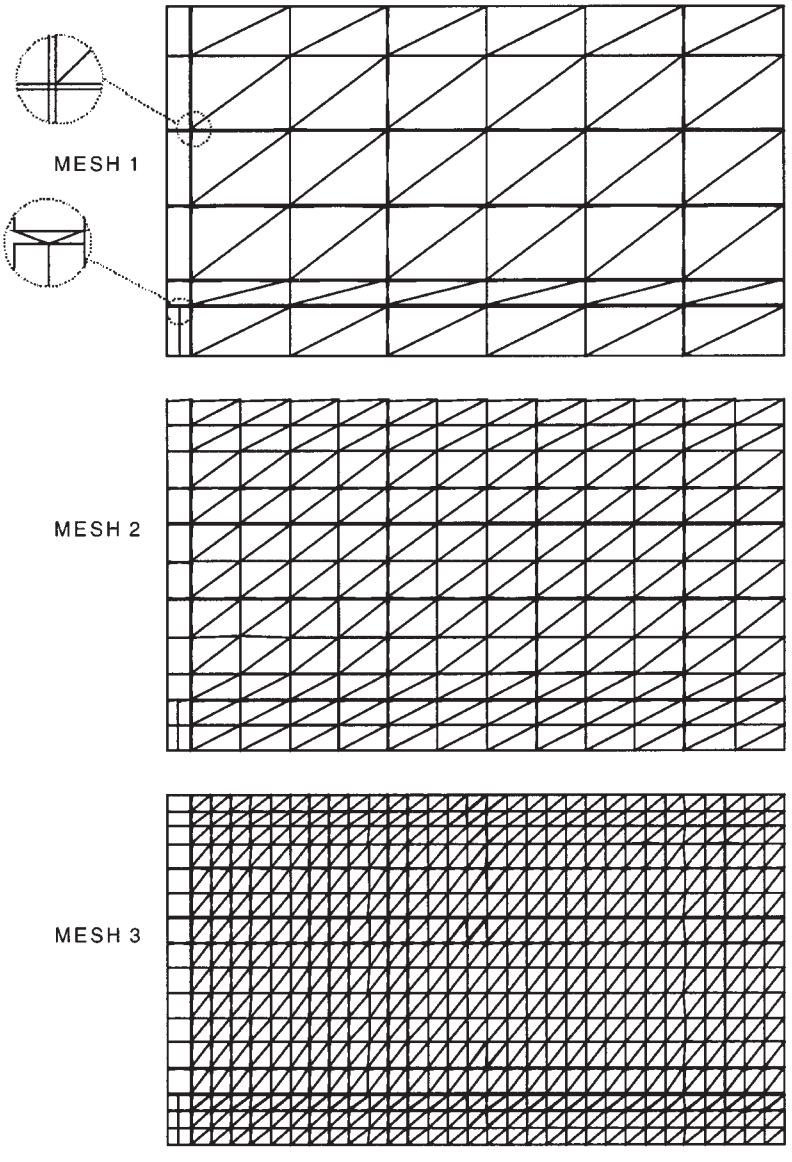

Figure 7. FE meshes for geogrid-reinforced wall simulation.

Table I. Data for mesh sensitivity studies.

Mesh No.	No. of Nodes	No. of soil elements	No. of wall elements	No. of geogrid elements	No. of interface elements
1	142	108	12	28	7
2	314	336	18	52	12
3	858	1140	24	124	17

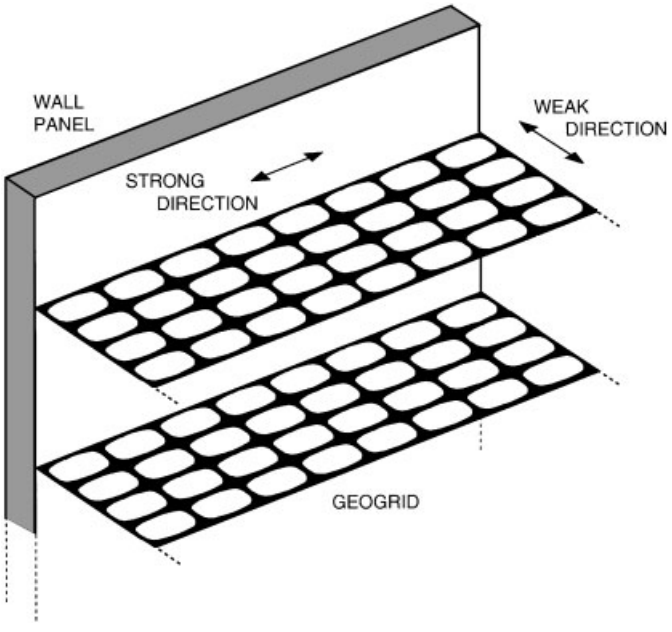

Figure 8. Perspective view of GRS wall showing features of geogrid reinforcement.

The simulation proceeded as follows. First, a gravity load corresponding to a soil unit weight of $\gamma = 17.5\ \mathrm{kN/m^3}$ was turned on, vertically compressing the soil elements behind the wall and causing the geogrids to move along with the soil. Since the geogrids were firmly attached to the wall, they sagged more behind the wall. This expected deviation of geogrids from perfect alignment was captured by updating the nodal coordinates of the mesh after the gravity loading phase and using these new coordinates in subsequent analysis. After the initial condition has been established, surcharge loads were applied on the ground surface in the form of equivalent nodal forces. During this stage the retaining wall deflected laterally, stretching the soil behind it as well as the geosynthetic reinforcements embedded in the soil. The wall deflection reflects a rotational mechanism about the toe since the bottom of the wall is pinned to the base support. The structural response can be conveniently reported in the form of horizontal wall deflection as a function of intensity of surcharge.

A critical component of the FE model is an interface layer between the soil and the back face of the wall. In the simulations we used a friction angle of $\phi_{sw} = 20^\circ$ for the soil–wall interface as suggested in Reference [37]. The soil–wall interface layer was modelled using continuum elements with a DP frictional parameter of $\beta = 0.10$ and zero dilation angle. The interface

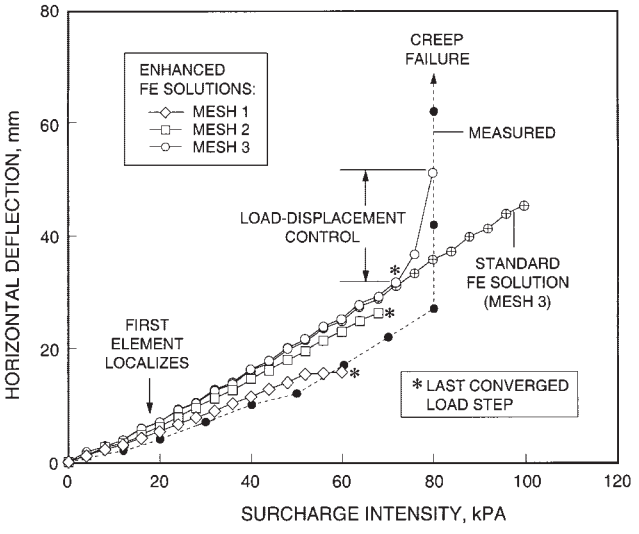

Figure 9. Mesh sensitivity studies. Predictions assume geogrids are stretched in weak direction.

elements simply allow the soil to move tangentially relative to the wall (without dilation) once the threshold friction angle value has been reached. Since this interface layer is so thin and is subjected to horizontal compressive normal stresses, a value of Poisson's ratio close to 0.5 has been specified so that it would become incompressible and thus prevent the wall and soil elements from overlapping. Potential numerical problems associated with mesh locking for incompressible FE applications were avoided by using the B-bar method [62] for the interface elements.

As noted earlier, a Tensar SS1 geogrid was used for the reinforcements and has been chosen so that the reinforcement would fail under the current surcharge loads. Stiffness properties of this geogrid typically vary with elongational strains. Manufacturers literature reported a gross elastic stiffness of about 204 kN/m in the weak direction and 292 kN/m in the strong direction, both measured at 2% strain [21]. Part of the FE analysis deals with the investigation of the effect of the geogrid stiffness on the horizontal wall deflection.

A unique feature of the present work is the localization analysis that renders the boundary-value problem well-posed at all times. As noted in the preceding section, a standard FE analysis in the unstable regime creates spurious mesh sensitivities due to the loss of ellipticity of the field equations. Thus, once an element localizes its displacement interpolation is enhanced by embedding a discontinuity to resolve the steep gradient across the band. As noted in Reference [22], the enhancement may be either in the form of an embedded continuum or an embedded slip plane, and in this work we embed a slip plane. The post-localized constitutive response on the slip plane is then given by the new yield function

$$\mathscr{G} = (\mathbf{n} \otimes \boldsymbol{\mu}) : \boldsymbol{\sigma} - c_{\mathscr{S}} = 0, \quad \boldsymbol{\mu} = \mathbf{m} + \mathbf{n} \tan \phi_{\mathscr{S}} \tag{18}$$

where $\mathbf{m}$ is the unit vector in the direction of the instantaneous velocity jump, and $\phi_{\mathscr{S}}$ and $c_{\mathscr{S}}$ are, respectively, the mobilized friction angle and cohesion on the surface of discontinuity.

At post-localization a mobilized friction angle of $\phi_{\mathscr{S}} = 45^\circ$ is used, estimated from residual values obtained from direct shear tests and consolidated-drained triaxial tests [27]. The residual

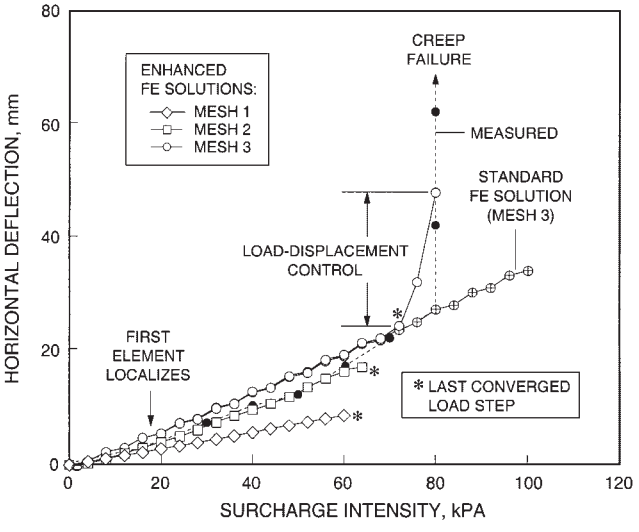

Figure 10. Mesh sensitivity studies. Predictions assume geogrids are stretched in strong direction.

mobilized cohesion is $c_{\mathscr{G}} = 0$, but the 'transient' value may be initially non-zero to provide a smooth transition from the pre-localized yield function $\mathscr{F}$. In other words, if $\boldsymbol{\sigma}^*$ denotes the stresses at the bifurcation point such that $\mathscr{F}(\boldsymbol{\sigma}^*) = 0$, then $c_{\mathscr{G}} = (\mathbf{n} \otimes \boldsymbol{\mu}) : \boldsymbol{\sigma}^* > 0$ defines the initial value of the cohesion on the interface so that $\mathscr{G}(\boldsymbol{\sigma}^*) = 0$ also at the bifurcation point (for consistency). The parameter $c_{\mathscr{G}}$ may then be made to gradually decay to zero with continued plastic activation of the band according to an assumed softening parameter $H_\delta = -100$ kPa. Note that the softening parameter simply reflects the rate at which the apparent cohesion on the band goes to zero, and does not affect the final residual response, see References [15–22].

MESH SENSITIVITY STUDIES

In this section we compare the predictions of the three FE meshes shown in Figure 7 and demonstrate convergence of the FE solutions with mesh refinement. From the same initial stress condition induced by the weight of the backfill soil, vertical surcharge loads in the form of equivalent nodal forces were applied on the ground surface in $\Delta q = 4$ kPa loading increments. The horizontal deflections resulting from these incremental loads are plotted in Figures 9 and 10, assuming the geogrids were oriented in the weak (true) and strong (hypothetical) directions, respectively. Also shown in Figures 9 and 10 are the stages in the solution where localization was first detected in each of the meshes (localization was first detected in the elements nearest to the pinned base of the wall). In all the runs the retaining wall was assumed to be rigid but can rotate freely about the pinned base.

The plots shown in Figures 9 and 10 demonstrate the expected trend that the finer mesh predicts a 'softer' behaviour because it is able to resolve the deformation pattern more accurately. However, between mesh 2 and mesh 3 the difference in the stiffness responses may be considered small. Note that this slight mesh dependency of the solution is associated with the standard FE interpolation and not a consequence of the embedded discontinuity approach.

Also note that coarser meshes failed to provide convergent solutions at earlier stages of loading since a larger finite element does entail a longer displacement discontinuity to be embedded each time a new localizing element is enhanced, which in turn influences the rate at which the shear band propagation is effectively captured by the mesh [20]. Note that the numerical model tends to overpredict the lateral wall deflections; this may be due to the test facility sidewalls contributing a small fraction to the total active force that would otherwise act in a true plane strain condition [21].

Mesh 3 (finest) failed to converge beyond a surcharge pressure intensity of $q = 72$ kPa in both runs shown in Figures 9 and 10. This is due to the tangent operator becoming nearly singular as the solution gets closer to the peak load, making it more difficult for the Newton iterations to converge. We have devised an artificial numerical strategy using a combined load-displacement control in an attempt to advance the solution further beyond the last convergent load step (and thus also show that the lack of convergence was not only numerical in nature but in fact is related to the physical instability occurring in the structure). The technique is to introduce a fictitious horizontal roller support at the top of the wall while applying the next incremental surcharge load, then move the fictitious roller support away from the wall to such a distance that the roller reaction produced from the previous load step vanishes. Effectively, each load increment beyond the last convergent load step is now applied in two subincrements. Caution must be taken in interpreting these additional results since the structure now follows a slightly different loading path. The technique generated two more points beyond the last convergent load step, which clearly show an accelerated softening response. This nearly unstable behaviour is corroborated by the measured horizontal wall deflections growing indefinitely with time at a sustained surcharge intensity of $q = 80$ kPa due to creep [21].

Also shown in Figures 9 and 10 are the predictions obtained from mesh 3 using standard FE approximations, i.e., without strain enhancements. The early stages of loading show nearly the same deformation responses as those predicted by the FE solution with strain enhancements; however, the standard FE model continues to provide convergent and stable solutions even beyond the 80 kPa ultimate load. In other words, the standard FE solution did not correctly predict when the failure of this structure would occur, much less what the nature of the collapse mechanism would be. As noted earlier, this is due to the fact that the standard FE approximation is restricted by the requirement that the deformation be conforming, and thus cannot predict the failure load and the accompanying collapse mechanism. It is also very likely that the standard FE solution in the advanced stages of deformation may have been corrupted by spurious mesh sensitivities making any interpretation of the predicted mechanism practically worthless. These shortcomings of the standard FE solution are clearly addressed by the enhanced FE model.

RESULTS AND DISCUSSIONS

Observations of numerous different failed GRS test walls reported in the literature have permitted identification of important mechanisms like strain localization, load redistribution effects in reinforcements, load transfer to the wall facing foundation, and sagging of the soil mass with arching effects in reinforcements to have a significant impact on the performance of these walls up to failure. As mentioned before, these mechanisms are typically not accounted for

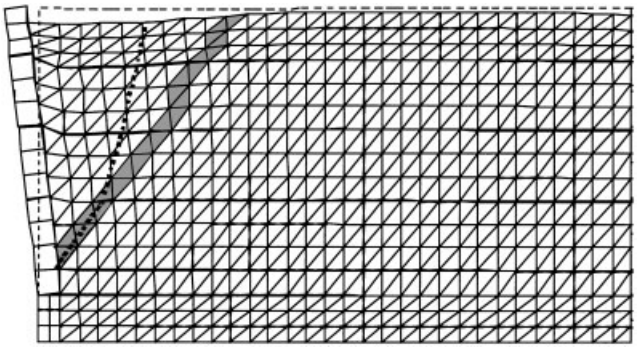

Figure 11. Deformed FE mesh at soil failure. Actual failure surface orientation shown as dashed curve while shaded elements represent localized elements. Deformations magnified $5\times$.

in traditional limit equilibrium methods [38, 39, 45]. In this section, we report how some of these features are captured by the proposed FE model.

Figure 11 shows a deformed FE mesh suggesting a concave upward shear band forming at the conclusion of the numerical simulation. Note that the shear band is allowed to propagate across the geogrid elements, which implies that the geogrid elements themselves must accommodate strain enhancements in the form of displacement jumps. Physically, this is a realistic proposition since the geogrids are so thin to have any significant shear stiffness, and since there is a significant area through and across the plane of the geogrids where the shear bands could possibly pass. The ability of the geogrid elements to accommodate a shear band is a critical component of the GRS wall FE model.

Also shown in Figure 11 is the orientation of an internal failure surface observed after careful excavation of the backfill. The observed orientation closely matches the computed one near the pinned base of the wall, but steepens up near the ground surface to an almost vertical slope. This may be due to the fact that the active wedge formed behind the wall is not an elastic zone but instead is characterized by a region of high straining where secondary slip surfaces formed and coalesced to alter the general orientation of the primary shear band. The high strains present behind the wall contradict a conventional assumption in limit equilibrium analysis that the active wedge translates as a rigid body.

To elaborate the last sentence of the previous paragraph, Plate 1 and Figure 12 show contours of conforming octahedral shear strains (in decimals) developing behind the wall at the conclusion of the numerical simulation. Conforming strains are obtained directly from the calculated nodal displacements using the standard linear strain-displacement operator $\mathbf{B}$. For standard finite elements, conforming strains represent the continuum strains in the elements, but for localized elements they must be added to the enhanced strains to obtain the total strains, which are singular on the slip surface. For both standard and enhanced FE solutions, the conforming octahedral shear strains appear very high near the wall–soil interface due to frictional effects on the back face of the wall; however, whereas the strains are diffuse everywhere in the standard solution, the enhanced solution show strain localization also developing on the shear band. The three-dimensional plot shows the conforming strains on the shear band to be lower than those in the elements directly behind the wall; however, it must be noted once again that these strains must be added to the enhanced part to obtain the total strains, which are infinite on the shear band.

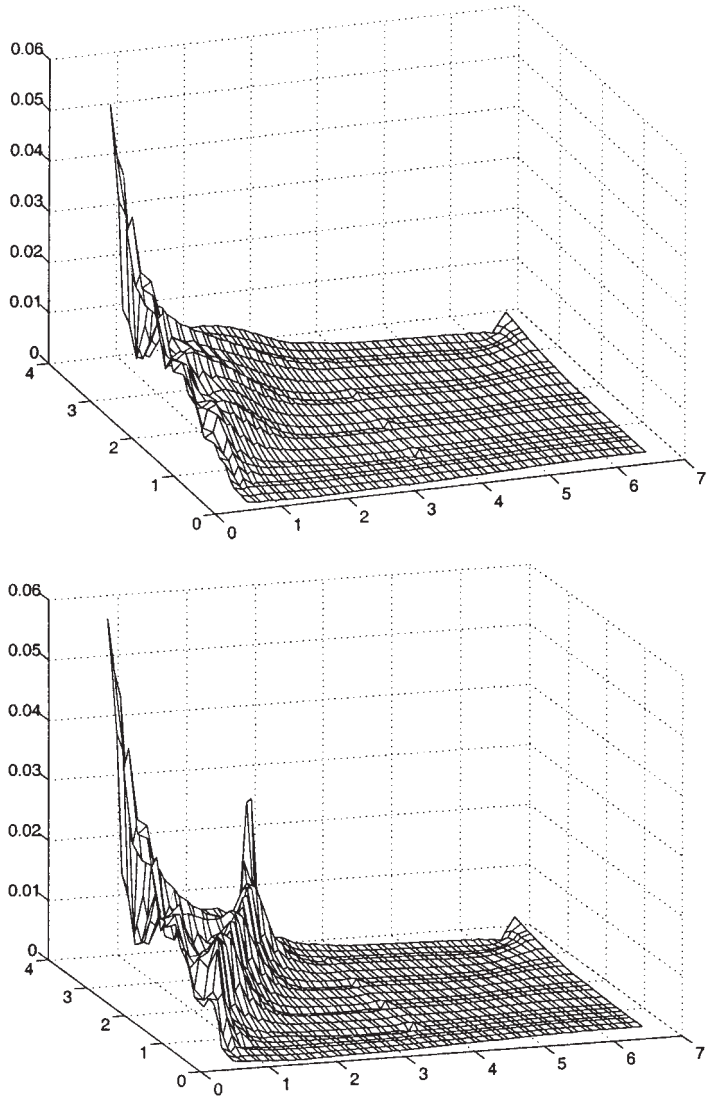

Figure 12. Conforming octahedral shear strains for standard (top) and enhanced (bottom) solutions.

Plate 2 and Figure 13 show contours of conforming volumetric strains (expansion is positive) developing behind the wall with and without strain enhancements. Again, the soil elements tend to dilate as they shear against the back face of the wall, resulting in high volumetric strains near the wall. Elsewhere, however, the volumetric strains calculated by the standard FE solution show a diffuse pattern, whereas the enhanced solution shows strain localization also developing on the shear band. The volumetric strains developing on the geogrid levels resulted directly from interpolating the axial elongation of the geogrids, which are stiffer than the surrounding soil elements and therefore experience lower volumetric strains. Throughout the course of the

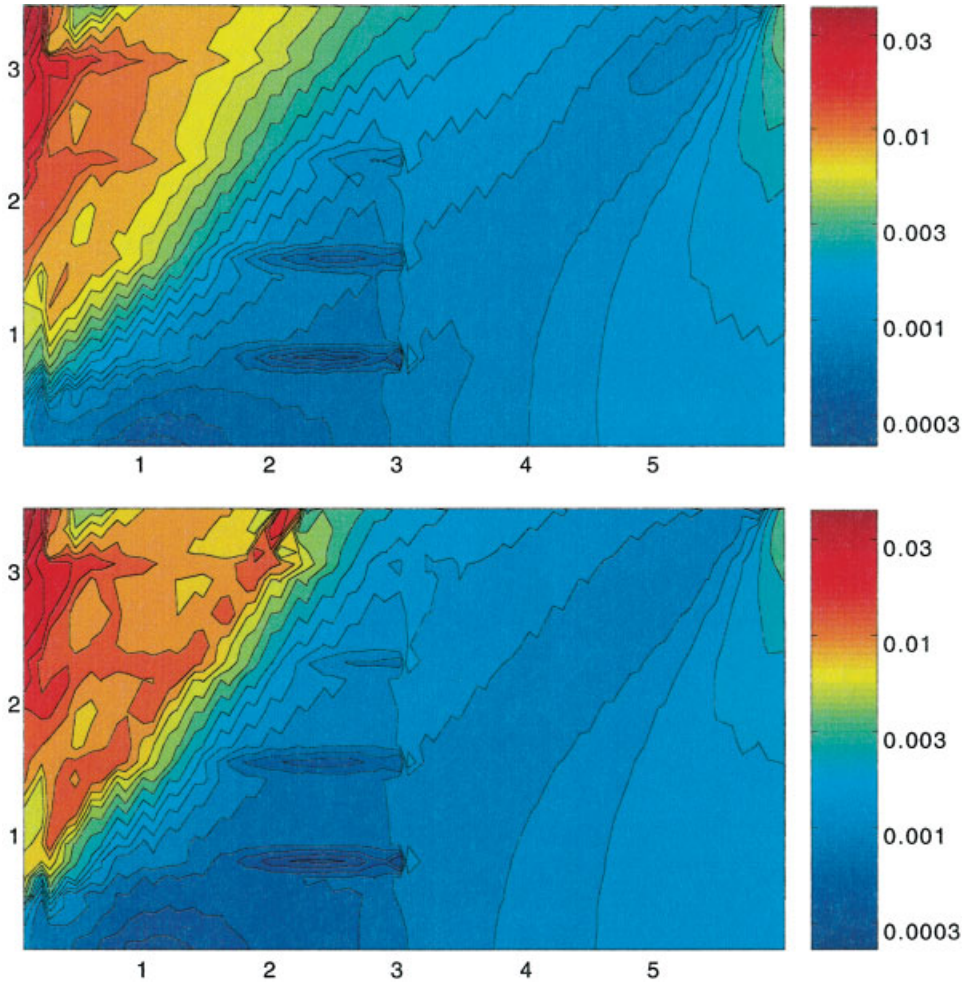

Plate 1. Conforming octahedral shear strains for standard (top) and enhanced (bottom) solutions.

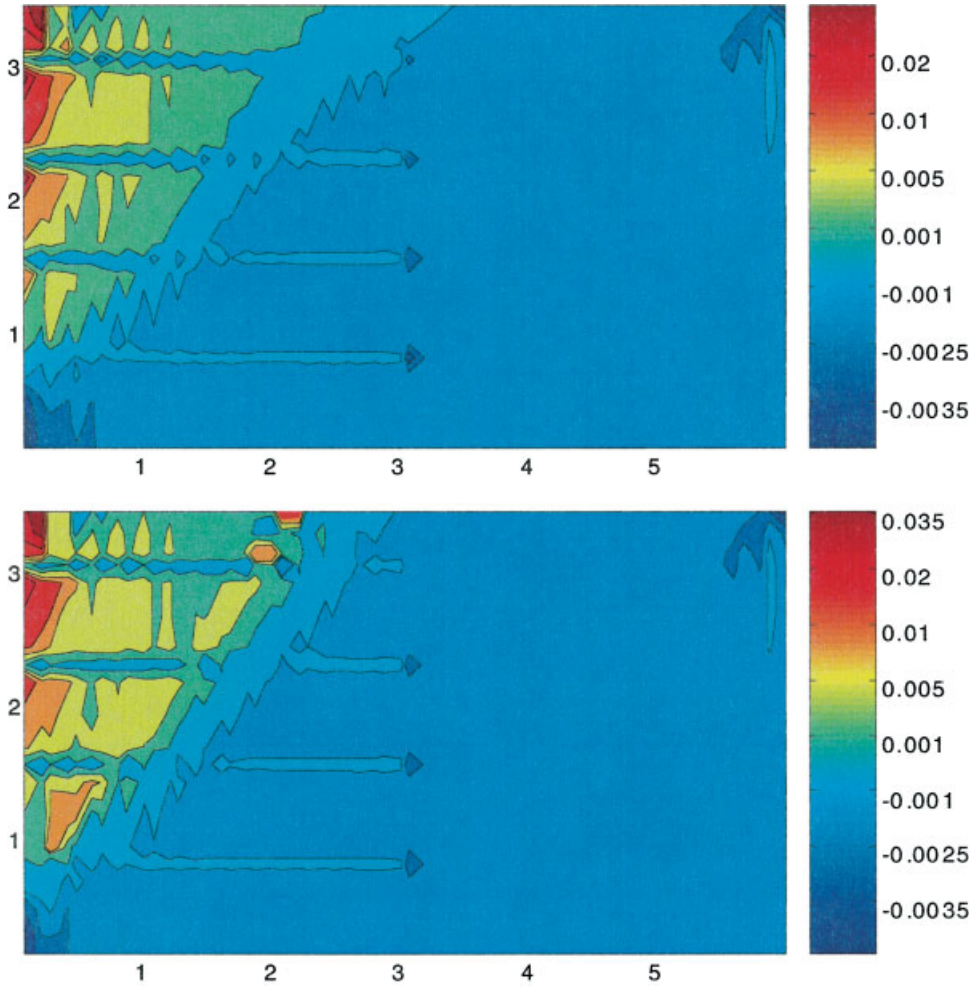

Plate 2. Conforming volumetric shear strains for standard (top) and enhanced (bottom) solutions.

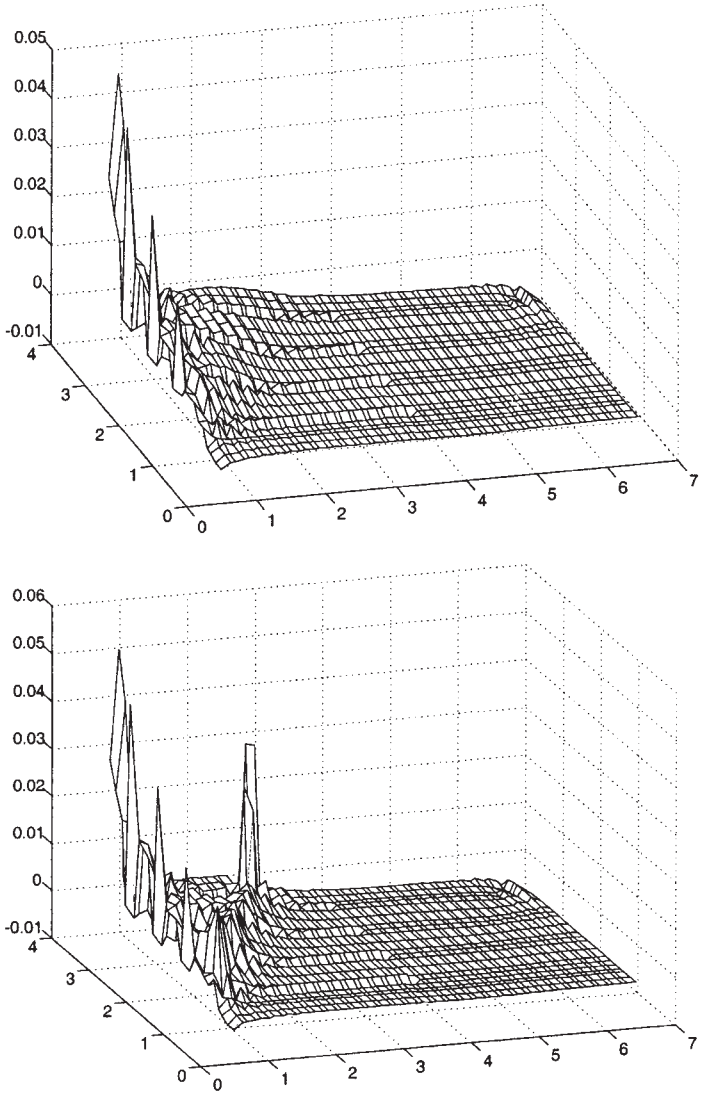

Figure 13. Conforming volumetric shear strains for standard (top) and enhanced (bottom) solutions.

numerical simulations many elements directly behind the wall have also satisfied the localization condition but have not been enhanced because they were not on the way of the primary shear band. Thus, the active wedge is not necessarily an intact zone but may be highly damaged by the presence of multiple shear bands.

Plots of tensile strains in the geogrids are shown in Figure 14. The measured values were taken at incipient soil failure prior to rupture of the topmost geogrid elements. Note that high tensile strains were measured nearer the wall. Caution must be taken in interpreting the numerical predictions relative to the measured strain values, since the initial conditions might not have been captured accurately by the numerical model. This is so because in reality soils behind the

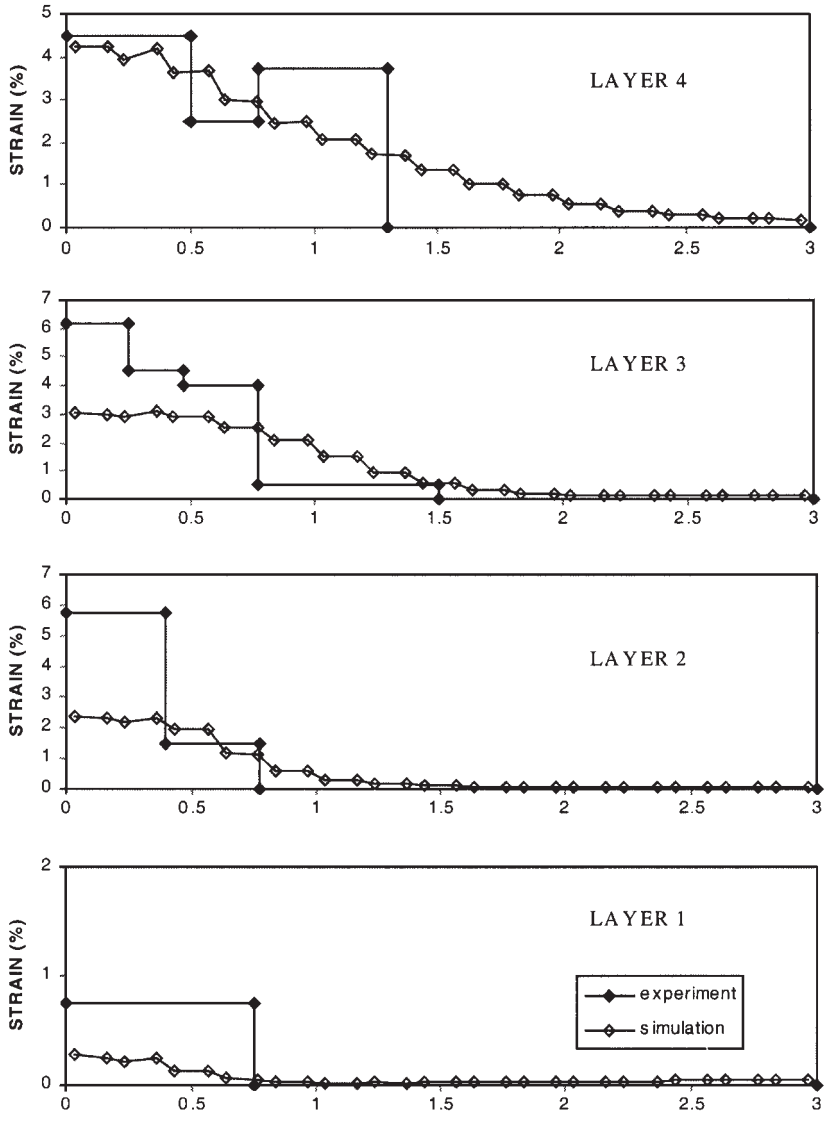

Figure 14. Axial strain in geosynthetic reinforcement layers at soil failure.

wall had been deposited in thin layers, whereas the numerical model did not simulate this complicated staged construction. Consequently, initial slacks and geometric irregularities in the geogrid configurations may have contributed to the equally irregular measured geogrid strain distributions. Nevertheless, the predicted axial strain distributions appear to be consistent with the measured values, with higher strain values also calculated near the wall.

The predicted and measured lateral wall deflections at the conclusion of the experiment (80 kPa surcharge loading) are shown in Figure 15. All values were adjusted relative to the deformed profiles prior to the imposition of the very first surcharge load increment. The measured profiles exhibited strong time-dependence, with the soil creeping to failure until the

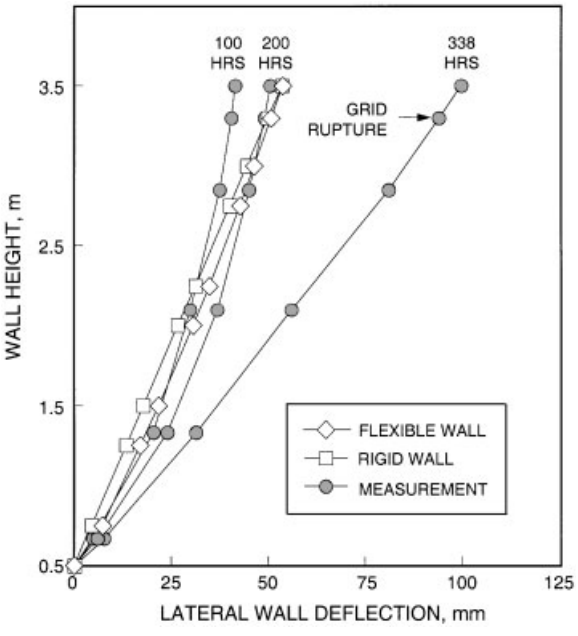

Figure 15. Cumulative wall deflections at end of surcharge loading.

geogrid ruptured after 338 h of sustained loading. As for the predictions, two walls with high and low flexural rigidities were tested, and the calculated wall deflection profiles are also shown in Figure 15. Clearly, the profile exhibited by the rigid wall defines a straight line; however, even with a flexible wall the solution is unable to capture the arching or bowing of the wall near the pinned base. This is due to the lack of capability of the CST and linear quadrilateral finite elements to capture bending modes near the pinned base of the wall. In addition to the sidewall friction effect alluded to earlier, this factor also could have been responsible for the horizontal wall displacements slightly being overpredicted near the top (cf. Figures 9 and 10), and for the geogrid tensile strains being underpredicted near the pinned base (cf. Figure 14).

Work is currently in progress aimed at developing more robust, higher-order elements (e.g., nine-noded Lagrangian elements) capable of capturing both bending modes and strong-discontinuity strain enhancements for strain localization analysis. To the knowledge of the authors, only the CST elements have so far been used routinely in conjunction with the embedded strong discontinuity approach, although attempts to use enhanced four-node quadrilateral elements also have proved successful [16–18]. However, as in conventional FE analysis more tests are needed before any enhanced higher-order elements can be used routinely for solving strain localization problems.

SUMMARY AND CONCLUSIONS

We have presented a FE methodology for analysing shear and volumetric strain localization behind a GRS test wall. The solution is based on a recently developed embedded displacement

discontinuity approach in which the strain interpolations in the localizing elements are enhanced following the satisfaction of a so-called localization condition. The paper highlights the deficiency of standard FE approximations in capturing strain localization effects and in predicting the failure load, in that it was unable to predict failure conditions because it lacked capability to resolve the intense deformations on the failure surface. In contrast, the proposed enhanced FE solutions predicted the ultimate load reasonably well, and captured the orientation of the primary shear band during the early stage of its development.

Results of the simulations suggest that the shear band initiated in soil elements near the pinned base of the test wall and propagated upward to the ground surface. However, this is not the only shear band possible. The active wedge is not necessarily an intact zone, contrary to a conventional assumption inherent in limit equilibrium-type analyses. Instead, this region is potentially a highly damaged zone where secondary shear bands are also likely to develop. Depending on the boundary and loading conditions, as well as on the material parameters, the primary shear band can initiate anywhere in the highly stressed zone of the structure. Accurate representation of all these factors is crucial to an accurate prediction of failure and near-failure behaviour of GRS walls.

As a more general result, the paper also highlights the potential fundamental inconsistencies with using the failure friction angle as the yield friction angle. Analyses have shown that at the failure friction angle it is possible for the non-associated Drucker–Prager, Lade–Duncan, and Matsuoka–Nakai plasticity models to define elastic regions that extend beyond the boundaries of the stable region, in which case ellipticity of the field equations is lost right at the moment of yielding. Because these plasticity models are typical of those used in practice, it would not be unreasonable to extrapolate this statement to other non-associated plasticity models as well, particularly those exhibiting a high degree of non-associativity. The assumption that the yield and failure friction angles are the same has been used traditionally to analyse collapse and near-collapse conditions in conjunction with the standard FE method; this paper shows that such 'standard' analysis may be deficient due to an ill-posed boundary-value problem leading to spurious mesh sensitivities of the standard FE solutions.

ACKNOWLEDGEMENTS

Financial support for this research was provided by National Science Foundation under Contract No. CMS-9700426. Funding for the third author was provided by a research assistantship from the John A. Blume Earthquake Engineering Center. The writers are grateful to Dr. Sunil S. Kishnani for providing the design properties of the geogrids.

REFERENCES

1. Armero F, Garikipati K. Recent advances in the analysis and numerical simulation of strain localization in inelastic solids. In *Proceedings of Computational Plasticity IV*, Owen DRJ, Oñate E, Hinton E (eds). CIMNE: Barcelona, Spain 1995; 547–561.
2. Adachi T, Oka F, Yashima A. A finite element analysis of strain localization for soft rock using a constitutive equation with strain softening. *Archive of Applied Mechanics* 1991; **61**:183–191.
3. Bazant ZP, Pijaudier-Cabot G. Nonlocal continuum damage, localization instability and convergence. *Journal of Applied Mechanics* 1988; **55**:287–293.
4. de Borst R, Mühlhaus HB. Gradient-dependent plasticity: Formulation and algorithmic aspects. *International Journal for Numerical Methods in Engineering* 1992; **35**:521–539.
5. de Borst R, Pamin J, Sluys LJ. Computational issues in gradient plasticity. In *Continuum models for materials with microstructure*, Mühlhaus HB (ed.). Wiley: New York, 1995; 159–200.

6. Larsson R, Runesson K, Ottosen NS. Discontinuous displacement approximation for capturing plastic localization. *International Journal for Numerical Methods in Engineering* 1993; **36**:2087–2105.
7. Oka F, Yashima A, Sawada K, Aifantis EC. Instability of gradient-dependent elastoviscoplastic model for clay and strain localization analysis. *Computer Methods in Applied Mechanics and Engineering* 2000; **183**:67–86.
8. Ortiz M, Leroy Y, Needleman A. A finite element method for localized failure analysis. *Computer Methods in Applied Mechanics and Engineering* 1987; **61**:189–214.
9. Perić D, Runesson K, Sture S. Prediction of plastic localization using MRS-Lade model. *Journal of Geotechnical Engineering*, *ASCE* 1993; **119**:639–661.
10. Perić D, Runesson K, Sture S. Evaluation of plastic bifurcation for plane strain versus axisymmetry. *Journal of Engineering Mechanics*, *ASCE* 1992; **118**:512–524.
11. Simo JC, Oliver J, Armero F. An analysis of strong discontinuities induced by strain-softening in rate-independent inelastic solids. *Computational Mechanics* 1993; **12**:277–296.
12. Viggiani G, Finno RJ, Harris WW. Experimental observations of strain localisation in plane strain compression of a stiff clay. In *Localization and bifurcation theory for soils and rocks*, Chambón R, Desrues J, Vardoulakis I (eds). Balkema: Rotterdam, 1994; 189–198.
13. Wan RG, Chan DH, Morgenstern NR. A finite element method for the analysis of shear bands in geomaterials. *Finite Elements in Analysis and Design* 1990; **7**:129–143.
14. Zienkiewicz OC, Pastor M, Huang M. Softening, localisation and adaptive remeshing. Capture of discontinuous solutions. *Computational Mechanics* 1995; **17**:98–106.
15. Borja RI. A finite element model for strain localization analysis of strongly discontinuous fields based on standard Galerkin approximation. *Computer Methods in Applied Mechanics and Engineering* 2000; **190**:1529–1549.
16. Borja RI, Regueiro RA. Strain localization in frictional materials exhibiting displacement jumps. *Computer Methods in Applied Mechanics and Engineering* 2001; **190**:2555–2580.
17. Regueiro RA, Borja RI. Plane strain finite element analysis of pressure-sensitive plasticity with strong discontinuity. *International Journal of Solids and Structures* 2001; **38**:3647–3672.
18. Regueiro RA, Borja RI. A finite element model of localized deformation in frictional materials taking a strong discontinuity approach. *Finite Elements in Analysis and Design* 1999; **33**:283–315.
19. Borja RI, Regueiro RA, Lai TY. FE modeling of strain localization in soft rocks. *Journal of Geotechnical and Geoenvironmental Engineering*, *ASCE* 2000; **126**:335–343.
20. Borja RI, Lai TY. Propagation of localization instability under active and passive loading. *Journal of Geotechnical and Geoenvironmental Engineering*, *ASCE* 2002; **128**:64–75.
21. Bathurst RJ, Benjamin, DJ. Failure of a geogrid-reinforced soil wall. *Transportation Research Record* 1990; **1288**:109–116.
22. Borja RI. Finite element simulation of strain localization with large deformation: Capturing strong discontinuity using a Petrov-Galerkin multiscale simulation. *Computer Methods in Applied Mechanics and Engineering* 2002; **191**:2949–2978.
23. Michalowski RL. Plasticity-based analysis of reinforces soil structures. In *Advances in Systems Using Geosynthetics*, Zornberg JG, Christopher BR (eds). ASCE Geotechnical Special Publication No. 103, 2000; 346–359.
24. Meehan RL, Karp LB. California housing damage related to expansive soils. *Journal of Performance of Constructed Facilities* 1994; **8**:139–157.
25. Adib M, Mitchell JK, Christopher BR. Finite element modeling of reinforced soil walls and embankments. *Proceedings of the ASCE Conference on Design and Performance of Earth Retaining Structures*. New York, 1990; 409–423.
26. Bathurst RJ, Koerner RM. Results of class A predictions for the RMC reinforced soil wall trials. In *The Application of Polymeric Reinforcement in Soil Retaining Structures*, Jarrett P, McGown A (eds). Kluwer Academic Publishers: Dordrecht, 1987; 127–171.
27. Bathurst RJ, Wawrychuk W, Jarrett P. Laboratory investigation of two large-scale geogrid reinforced soil walls. In *The Application of Polymeric Reinforcement in Soil Retaining Structures*, Jarrett P, McGown A (eds). Kluwer Academic Publishers: Dordrecht, 1987; 75–125.
28. Bathurst RJ, Walters D, Vlachopoulos N, Burgess P, Allen TM. Full-scale testing of geosynthetic reinforced walls. In *Advances in Transportation and Geoenvironmental Systems Using Geosynthetics*, Zornberg JG, Christopher BR (eds). ASCE Geotechnical Special Publication No. 103, 2000; 201–217.
29. Bauer A, Bräu G. Backanalyses of a steep slope reinforced with nonwovens. In *Geosynthetics*: *Applications*, *Design and Construction*, DeGroot MB, Den Hoedt G, Temaat RJ (eds). Balkema: Rotterdam, 1996; 225–228.
30. Bergado DT, Long PV, Werner G. Deformation behavior of geotextile reinforcement at vicinity of shear surface. In *Geosynthetics*: *Applications*, *Design and Construction*, DeGroot MB, Den Hoedt G, Temaat RJ (eds). Balkema: Rotterdam, 1996; 177–182.
31. Carrubba P, Luchetta F, Montanelli F, Moraci N. Instrumented reinforced wall: Measurements and FEM results. In *Advances in Systems Using Geosynthetics*, Zornberg JC, Christopher BR (eds). ASCE Geotechnical Special Publication No. 103, 2000; 271–291.

32. Chang DT, Hung FY, Sun TS. Laboratory study and numerical analysis for pull-out behaviors of geogrids confined by weathered mudstone and sandy soil. In *Geosynthetics*: *Applications*, *Design and Construction*, DeGroot MB, Den Hoedt G, Temaat RJ (eds). Balkema: Rotterdam, 1996; 217–224.
33. Chou NS. Present design problems and finite element method study on performance of geosynthetic-reinforced soil retaining walls. In *Recent Case Histories of Permanent Geosynthetic-Reinforced Soil Retaining Walls*, Tatsuoka F, Leshchinsky D (eds). Balkema: Rotterdam, 1994; 117–130.
34. Christopher BR, Bonczkiewicz C, Holtz RD. Design, construction and monitoring of full scale test of reinforced soil walls. In *Recent Case Histories of Permanent Geosynthetic-Reinforced Soil Retaining Walls*, Tatsuoka F, Leshchinsky D (eds). Balkema: Rotterdam, 1994; 45–60.
35. Handel E, Schweiger HF, Yeo KC. A simple thin-layer element to model soil-geotextile interaction. *Performance of Reinforced Soil Structures*, British Geotechnical Society, 1990; 317–321.
36. Jaber M, Mitchell JK, Christopher BR. Finite element modeling of reinforced soil walls and embankments. *Proceedings of the ASCE Conference on Design and Performance of Earth Retaining Structures*. New York, 1990; 409–423.
37. Karpurapu R, Bathurst RJ. Behaviour of geosynthetic reinforced soil retaining walls using the finite element method. *Computers and Geotechnics* 1995; **17**:279–299.
38. Leshchinsky D. Stability of geosynthetic reinforced steep slopes. In *Proceedings of the International Symposium on Slope Stability Engineering*, vol. 1, Yagi N, Yamagami T, Jiang JC (eds). Balkema: Rotterdam, 1990; 463–479.
39. Leshchinsky D. Performance of geosynthetic reinforced slopes at failure—Discussion. *Journal of Geotechnical and Geoenvironmental Engineering*, *ASCE* 2000; **126**:281–283.
40. Ochiai Y, Fukuda N. Experimental study on geotextile-reinforced soil walls with different facings. In *Geosynthetics*: *Applications*, *Design and Construction*, DeGroot MB, Den Hoedt G, Temaat RJ (eds). Balkema: Rotterdam, 1996; 113–120.
41. Rowe KR, Ho SK. Some insights into reinforced wall behaviour based on finite element analysis. In *Geosynthetics*: *Applications*, *Design and Construction*, DeGroot MB, Den Hoedt G, Temaat RJ (eds). Balkema: Rotterdam, 1996; 485–490.
42. Wong KS, Broms, BB. Failure modes at model tests of a geotextile reinforced wall. *Geotextiles and Geomembranes* 1994; **13**:475–493.
43. Yokota Y, Nakane A, Taki T, Miyatake H. FEM comparative analysis of facing rigidity of geotextile-reinforced soil walls. In *Geosynthetics*: *Applications*, *Design and Construction*, DeGroot MB, Den Hoedt G, Temaat RJ (eds). Balkema: Rotterdam, 1996; 433–438.
44. Zornberg JG, Sitar N, Mitchell JK. Performance of geosynthetic reinforced slopes at failure. *Journal of Geotechnical and Geoenvironmental Engineering*, *ASCE* 1998; **124**:670–683.
45. Zornberg JG, Sitar N, Mitchell JK. Limit equilibrium as basis for design of geosynthetic reinforced slopes. *Journal of Geotechnical and Geoenvironmental Engineering*, *ASCE* 1998; **124**:684–698.
46. Vermeer PA, de Borst R. Nonassociated plasticity for soils, concrete and rock. *Heron* 1984; **29**:1–64.
47. Drucker DC, Prager W. Soil mechanics and plastic analysis or limit design. *Quarterly of Applied Mathematics* 1952; **10**:157–165.
48. Borja RI. *Plasticity Modeling and Computation*. Lecture Notes: Stanford University, 2002.
49. Lade PV, Duncan JM. Elastoplastic stress-strain theory for cohesionless soil. *Journal of Geotechnics and Engineering Division*, *ASCE* 1975; **101**:1037–1053.
50. Matsuoka H, Nakai T. Stress-deformation and strength characteristics of soil under three different principal stresses. *Proceedings of JSCE* 1974; **232**:59–70.
51. Borja RI, Sama KM, Sanz PF. On the numerical integration of three-invariant elastoplastic constitutive models. *Computer Methods in Applied Mechanics and Engineering* 2003; **192**: 1227–1258.
52. Borja RI, Tamagnini C. Cam-Clay plasticity, Part III: Extension of the infinitesimal model to include finite strains. *Computer Methods in Applied Mechanics and Engineering* 1998; **155**:73–95.
53. Borja RI, Lin CH, Montáns FJ. Cam-Clay plasticity, Part IV: Implicit integration of anisotropic bounding surface model with nonlinear hyperelasticity and ellipsoidal loading function. *Computer Methods in Applied Mechanics and Engineering* 2001; **190**:3293–3323.
54. Tamagnini C, Castellanza R, Nova R. A Generalized Backward Euler algorithm for the numerical integration of an isotropic hardening elastoplastic model for mechanical and chemical degradation of bonded geomaterials. *International Journal for Numerical and Analytical Methods in Geomechanics* 2002; **26**:963–1004.
55. Lade PV. Elasto-plastic stress-strain theory for cohesionless soil with curved yield surfaces. *International Journal of Solids and Structures* 1977; **13**:1019–1035.
56. Rudnicki JR, Rice JR. Conditions for the localization of deformation in pressure-sensitive dilatant materials. *Journal of the Mechanics and Physics of Solids* 1975; **23**:371–394.
57. Borja RI. Bifurcation of elastoplastic solids to shear band mode at finite strain. *Computer Methods in Applied Mechanics and Engineering* 2002; **191**:5287–5314.
58. Runesson K, Ottosen NS, Perić D. Discontinuous bifurcations of elastic-plastic solutions at plane stress and plane strain. *International Journal of Plasticity* 1991; **7**:99–121.

59. Ogden RW. *Non-linear Elastic Deformations*. Dover: New York, 1997.
60. Lambe TW, Whitman RV. *Soil Mechanics*. Wiley: New York, 1969.
61. Arthur JRF, Dunstan T, Al-ani QALJ, Assadi A. Plastic deformation and failure in granular media. *Géotechnique* 1977; **27**:53–74.
62. Hughes TJR. *The Finite Element Method*. Prentice-Hall: New Jersey, 1987.

